Supplementary Information to "Common microscopic origin of the phase transitions in Ta_2NiS_5 and the excitonic insulator candidate Ta_2NiSe_5"

Lukas Windgätter[1*], Malte Rösner[2], Giacomo Mazza[6], Hannes Hübener[1], Antoine Georges[3,4,5,6], Andrew J. Millis[5,7], Simone Latini[1*] and Angel Rubio[1,5,8*]

[1]Max Planck Institute for the Structure and Dynamics of Matter, Luruper Chaussee 149, 22761 Hamburg, Germany.
[2] Radboud University, Institute for Molecules and Materials, Heijendaalseweg 135, 6525 AJ Nijmegen, Netherlands.
[6]Department of Quantum Matter Physics, University of Geneva, Quai Ernest-Ansermet 24, 1211 Geneva, Switzerland.
[3]Collège de France, 11 place Marcelin Berthelot, 75005 Paris, France.
[4] Center for Computational Quantum Physics, Flatiron Institute, New York, New York 10010, USA.
[5] CPHT, CNRS, Ecole Polytechnique, IP Paris, F-91128 Palaiseau, France.
[7]Department of Physics, Columbia University, New York, New York 10027, USA.
[8]Nano-Bio Spectroscopy Group, Departamento de Física de Materiales, Universidad del País Vasco, 20018 San Sebastian, Spain.

*Corresponding author(s). E-mail(s): lukas.windgaetter@mpsd.mpg.de; simone.latini@mpsd.mpg.de; angel.rubio@mpsd.mpg.de;

Supplementary Note 1

The bandstructures have been computed along the path M=$(\frac{\pi}{a}, 0, \frac{\pi}{c})$, Z=$(0, 0, \frac{\pi}{c})$, Γ=$(0, 0, 0)$ and X=$(\frac{\pi}{a}, 0, 0)$.

Supplementary Note 2: Total energy minimum with different functionals

To track the total energy changes during the relaxation for different functionals we have computed the energy of the system along the structural transition. We employed again the d parameter introduced in section 2.4 of the main text to parameterize the transition. The resulting total energy vs d distortion graph is shown in Supplementary Figure 1. For all functionals the total energy is displayed with the orthorhombic value set 0 eV. The figure shows, that using the PBE functional has the energy minimum at slightly lower values for the distortion and the HSE has its energy minimum at stronger distortion values of d. Nevertheless, a monoclinic structure is energetically more stable than the orthorhombic geometry for all investigated functionals.

Supplementary Note 3: Spin-Orbit Coupling

The results for the PBE, mBJ and HSE03 with and without Spin-Orbit Coupling (SOC) functional are shown in the Supplementary Figures 2, 3 and 4. They show that SOC leads to a bandsplitting which is most apparent on the M-Z path for all band dispersions. Note, that this band splitting is not a splitting of spin up and down states. Near the bandedge the spin orbit coupling has just a small influence on the bandstructures. Only for the monoclinic geometry of TNSe using the PBE functional changes are apparent with the bandgap halving and the becoming and direct at Γ. A detailed comparison of the obtained bandgaps is presented in Supplementary Table 6. We conclude, that the effects of SOC are negligible for our discussion in the main text. These results are in agreement with a prior study by Sugimoto et al. [1].

Supplementary Note 4: Increasing the exchange-correlation contribution in the functionals

Increasing the exchange and correlation contribution considered in either the HSE hybrid functionals or the modified-Becke-Johnson functional will lead to a bandgap opening even in the orthorhombic unit cell. In the modified Becke-Johnson (mBJ) functional the amount of exchange and correlation interaction included is controlled by the c parameter. It controls the amount of Becke-Roussel exchange [2, 3], which approximates exact exchange effects via an effective potential, plus a screening term [4]. In the HSE hybrid functionals the exact exchange contribution is calculated directly using the Kohn-Sham orbitals during the self consistent iterations. Parts of the PBE exchange interaction are replaced by the exact exchange interaction [5]. The admixture of

exact and PBE exchange in the functional is controlled by the mixing parameter α which is commonly set to 0.25 for the HSE functionals. Varying it we can modify the amount of exchange interaction analogously to varying the c parameter in the mBJ functional. The results are shown in the Supplementary Figure 5 and Supplementary Figure 6. We see, that for values of c =1.6 or higher a bandgap opens, while the system is still metallic for the self consistently calculated c-Value of 1.26. Analogously we can control the amount of exchange and correlation included in the range separated hybrid functionals. To test this we have varied the mixing parameter α, while keeping the range separation parameter at 0.3. This way $\alpha = 0.25$ reproduces the result for the HSE03 functional. The resulting bandstructures can be seen in Supplementary Figure 6. The behaviour is similar to the mBJ case, with the orthorhombic cell becoming a semiconductor for values of $\alpha > 0.45$.

Supplementary Note 5: Minimally symmetry broken electron dispersion

We used the displacement parameter d as defined in section 3 of the main text to introduce a minimal distortion to the lattice (d=0.05). This procedure breaks the relevant orthorhombic lattice symmetries. If the phase transition of TNSe is fully electronic the breaking of the symmetries should already induce the metal to semiconductor transition. The result for the electronic dispersion of the symmetry broken geometry is shown in Supplementary Figure 8. We see that all bandstructures ,independent of the exchange correlation functional, do not exhibit a metal to insulator transition or a significant gap opening. In fact they agree very well with the exact orthorhombic results.

Supplementary Note 6: STS Gap Correction

In STS measurements a metal to semiconductor transition has been reported at the critical temperature for TNSe [6]. The reported bandgap is 300 meV and is significantly bigger than the bandgap obtained from optics measurements of 160 meV [7]. The discrepancy can be explained taking the different geometries of the investigated samples of TNSe in account. The sample used for the STS measurement exhibits an β-angle of 92.5° and is such significantly bigger than the literature result of 90.5°-90.7° [8, 9]. To correct the bandgap taking this discrepancy into account, we computed the bandstructures for both our monoclinic unit cell as well as a unit cell with 92.5° β-angle. The obtained bandgaps are 40meV for our relaxed geometry and 66 meV for the 92.5° geometry using the PBE functional. Taking the ratio of these two and multiplying the 300 meV experimental gap, we obtain a correction of the STS gap to 181 meV.

Supplementary Note 7: Convergence of the G_0W_0 calculations

We present the details of the convergence of the G_0W_0 calculation for the monoclinic unit cell. To display the convergence behaviour of the calculation

we performed convergence studies for the number of k-Points needed in each direction, the number of unoccupied bands and the energy cutoff we have to consider for the response function calculation and size of the frequency grid of the frequency integration. It is important to note, that the energy cutoff for the response function and the number of unoccupied states are not independent convergence parameters and thus, we use the standard method and converge them simultaneously [10]. The bandstructures have been obtained via post-processing using the Wannier90 package [11].
For the presented convergence studies we have employed the Density Functional Theory solution using the PBE functional as starting point. A discussion of the effect using different functionals such as the HSE hybrid functional is in the section 2.3 of the main text.

For the bandstructure convergence of TNSe with varying k-mesh we will assume that the spatial directions for the k-mesh converge independently and perform a series of calculations with varying grid size in all three directions. To measure the convergence of the bandstructure we will compute the fundamental bandgap and extrapolate using a function $f(x) = a + b/(x + c)$ with a,b and c as fitting parameters. For these k-mesh calculations we used 640 unoccupied states with a 80eV Cutoff for the response function and 160 frequency grid points in the calculation of the screened interaction. The k-meshes are $k_x \times 4 \times 2$, $12 \times k_y \times 4$ and $12 \times 4 \times k_z$ with k_x, k_y and k_z are varied. The result is shown in Supplementary Figure 13. One sees, that the convergence in k_y and k_z along the corresponding reciprocal lattice directions converges quite fast. This is different for k_x as the bandstructure is highly dispersive in x-direction and many grid-points are needed to sample it accurately.

We also performed a simultaneous convergence of the energy cutoff for the response function and the number of unoccupied states. Convergence against the exact result should be in first order proportional to 1/Number of unoccupied states [10]. We have performed the convergence calculation in the standard way increasing response function cutoff and the number of included orbitals simultaneously. The given combinations are shown in Supplementary Table 8. The result of the energy convergence is presented in Supplementary Figure 14. We see, that including 1160 unoccupied states leads to a quite well converged bandgap already.

Lastly we also investigate of the convergence with increasing number of frequency grid points. This time the test setup is a k-mesh of 12x4x2 with 880 unoccupied states and a 100eV Cutoff. The result is shown in Fig 15. We see, that full convergence is only achieved for a large number of frequencies considered due to the small bandgap.

Supplementary Note 8: BSE Convergence

We also investigated the convergence behaviour of the solution of the Bethe-Salpether equation [12, 13] for the monoclinic phase of TNSe. We performed the BSE using the eigenenergies and screened interaction from the G_0W_0 calculation. The calculations show, that for all convergence parameters the excitonic

binding energy decreases proportional to the bandgap. This together with the fact, that even more converged G_0W_0 calculations in k_x tend to increase the G_0W_0 bandgap suggests, that for the material the excitonic binding energy does not exceed the bandgap. A detailed analysis of all relevant convergence parameters follows:

The solution of the Bethe-Salpether equation is very sensitive to the k-mesh. Thus, we investigated the solution of the BSE with an increasing k-mesh along the three different axes. We use a test setup with 160 frequencies for the calculation of the screened interaction, 640 unoccupied states (80eV cutoff) during the G_0W_0 calculation and include again the first 12 valence and 14 conduction bands in the BSE. The k-meshes used are k_xx4x2, 8xk_yx2 and 8x4xk_z, where k_x, k_y and k_z are variable and are be successively increased. The results are depicted in Supplementary Figure 16. We see, that while the dielectric function converges quickly with an increasing k-mesh in y-direction and z-direction, we need many k-points in k_x direction to obtain we reasonable result. The reason is, that the bandgap minimum is shifted slightly toward x-direction after the G_0W_0 calculation and therefore only very dense k-meshes can sample the highly dispersive energies in x-direction.

Secondly, we investigate the effect onto the BSE calculation for an increasing cutoff in the G_0W_0 calculation and an increasing number of unoccupied states. The test setup is working with a 12x4x2 k-mesh, 160 frequencies for the calculation of the screened interaction and including the first 12 valence and 14 conduction band states in the BSE. We employed the Tamm-Dancoff approximation [13, 14]. The results are depicted in Supplementary Figure 17. Using 880 unoccupied states with a 80eV cutoff already gives a well converged dielectric function and excitonic binding energies.

The third convergence parameter we investigate is the effect of including an increasing number of frequencies in the computation of the screened interaction onto the result of the Bethe-Salpeter equation. The test setup is using a 12x4x2 k-mesh, 640 unoccupied states and the first 12 valence and 14 conduction band states in the BSE. The results is depicted in Supplementary Figure 18. We see, that the BSE solution converges quite fast with the number of frequencies included in the calculation of the screened interaction. The dielectric function only obtains a rigid shift, which can be explained by the decreasing bandgap of the underlying G_0W_0 bandstructure calculation.

Lastly, we show the BSE convergence properties with an increasing number of valence and conduction bands included in the BSE calculation. The test setup includes a 12x4x2 k-mesh, 880 unoccupied states, a 80 eV cutoff and 160 frequencies in the calculation of the screened interaction. The number of valence (v) and conduction bands (c) included is varied. The convergence of the dielectric function and the eigenvalues of the BSE solution is displayed in the Supplementary Figure 19. We see, that we always obtain well converged eigenvalues, but need to include at least the first 12 valence and the first 14 conduction bands around the Fermi level to obtain a fully converged dielectric function. The excitonic eigenvalues are already very well converged only the first valence and conduction bands.

	a (in Å)	b (in Å)	c (in Å)
Experiment [9]	3.492	12.814	15.649
vdW-optB88	3.517	12.982	15.776
vdW-optPBE	3.532	13.325	15.845
PBE	3.510	14.160	15.776

Supplementary Table 1 Lattice parameters after full relaxation of the TNSe compound in the monoclinic phase using different functionals. The experimental reference data has been measured at 30K via X-ray diffraction [9]. The theory calculations are performed at T=0K.

	a (in Å)	b (in Å)	c (in Å)
Experiment[15]	3.503	12.870	15.677
vdW-optB88	3.512	12.993	15.771
vdW-optPBE	3.526	13.252	15.834
PBE	3.504	14.190	15.762

Supplementary Table 2 Lattice parameters after relaxation of the TNSe compound with enforced orthorhombic symmetry. The experimental values have been obtained via X-ray diffraction at T=400K [15]. The theory calculations are performed at T=0K.

	a (in Å)	b (in Å)	c (in Å)
Experiment[8]	3.415	12.146	15.097
orthorhombic	3.430	12.200	15.203
monoclinic	3.428	12.223	15.203

Supplementary Table 3 Lattice parameters for TNS of both the orthorhombic phase and the monoclinic phase obtained via full relaxation. The experimental values have been measured via X-ray diffraction at T=278 K. [8].

lattice vector	x (in Å)	y (in Å)	z (in Å)
a	3.51177786	0.00000000	0.00000000
b	1.75588893	6.49659343	0.00000000
c	0.00000000	0.00000000	15.77141641
species	a	b	c
Ta	0.22143275	0.55713450	0.88896088
Ta	0.22143275	0.55713450	0.61103912
Ta	0.77856725	0.44286550	0.11103912
Ta	0.77856725	0.44286550	0.38896088
Ni	0.70190352	0.59619297	0.75000000
Ni	0.29809648	0.40380703	0.25000000
Se	0.58116235	0.83767530	0.86174128
Se	0.58116235	0.83767530	0.63825872
Se	0.41883765	0.16232470	0.13825872
Se	0.41883765	0.16232470	0.36174128
Se	0.14695064	0.70609873	0.04873952
Se	0.14695064	0.70609873	0.45126048
Se	0.85304936	0.29390127	0.95126048
Se	0.85304936	0.29390127	0.54873952
Se	0.32729988	0.34540023	0.75000000
Se	0.67270012	0.65459977	0.25000000

Supplementary Table 4 Result of the relaxation of the orthorhombic cell with Cmcm symmetry obtained using the vdw-optB88 functional. The atoms are given in units of the lattice vectors a,b and c

lattice vector	x (in Å)	y (in Å)	z (in Å)
a	3.5172791481	0.0000000000	0.0000000000
b	1.7642919084	6.4903780477	0.0000000000
c	-0.1695581062	-0.0018790259	15.7763685968
species	a	b	c
Ta	0.788009744	0.446403261	0.888662426
Ta	0.765747213	0.446396149	0.611343122
Ta	0.209582861	0.558275853	0.111357977
Ta	0.231832330	0.558274801	0.388645515
Ni	0.297194687	0.407655269	0.750000961
Ni	0.701051209	0.596787458	0.250006008
Se	0.411119367	0.165767233	0.861499543
Se	0.424071823	0.165757101	0.638461393
Se	0.586395710	0.838882702	0.138539629
Se	0.573462842	0.838897364	0.361493392
Se	0.859540334	0.295478962	0.048418035
Se	0.845322448	0.295464258	0.451556475
Se	0.137960710	0.709232641	0.951592761
Se	0.152210287	0.709218409	0.548427477
Se	0.670947177	0.658753928	0.750003802
Se	0.327025141	0.345806896	0.249991137

Supplementary Table 5 Result of the relaxation of the triclinic cell using the vdw-optB88 functional. The atomic positions are given in units of the lattice vectors a,b, and c.

	TNSe, ortho	TNSe, mono	TNSe, ortho,SOC	TNSe, mono, SOC
PBE	metallic	40 meV	metallic	18 meV (-55%)
mBJ	metallic	101 meV	metallic	120 meV (+18%)
HSE03	metallic	183 meV	metallic	179 meV (-2%)
	TNS, ortho	TNS, mono	TNS, ortho,SOC	TNS, mono, SOC
PBE	metallic	102 meV	metallic	102 meV (+0%)
mBJ	42 meV	151 meV	98 meV (+133%)	178 meV (+18%)
HSE03	248 meV	352 meV	250 meV (+1%)	362 meV (+3%)

Supplementary Table 6 Comparison of the obtained bandgaps for TNSe and TNS with various functionals including SOC and neglecting it. We obtain quite good agreement between the SOC result and the non SOC result except for TNSe in the monoclinic phase for the PBE functional.

Mode	Orthorhombic (THz)	Monoclinic (THz)
1	-2.581	0.000
2	0.000	0.000
3	0.000	0.000
4	0.000	1.156
5	0.761	1.224
6	1.160	1.543
7	1.224	1.703
8	1.670	1.969
9	1.890	2.084
10	2.580	2.668
11	2.693	3.117
12	3.107	3.331
13	3.136	3.403
14	3.299	3.628
15	3.370	3.775
16	3.430	4.160
17	3.567	4.255
18	3.920	4.397
19	4.255	4.679
20	4.393	4.966
21	4.578	5.382
22	4.694	5.675
23	6.410	6.400
24	7.338	7.159
25	7.657	7.403
26	7.701	7.476
27	7.785	7.520
28	7.817	7.585
29	7.823	8.025
30	7.911	8.029
31	7.967	8.093
32	8.170	8.134
33	8.183	8.259
34	8.214	8.439
35	8.490	8.495
36	8.668	8.686
37	8.733	8.777
38	9.000	9.311
39	9.313	9.539
40	9.574	9.715
41	9.691	9.765
42	9.960	9.958
43	10.142	10.187
44	10.174	10.242
45	11.362	11.451
46	11.397	11.459
47	11.477	11.544
48	11.536	11.571

Supplementary Table 7 Eigenvalues of the phononic modes of TNS calculated at the Γ-Point.

cutoff (eV)	orbitals
60	640
80	880
100	1160
120	1480

Supplementary Table 8 Energy and orbital cutoff pairs used to check the convergence of the response function in the G_0W_0 calculation.

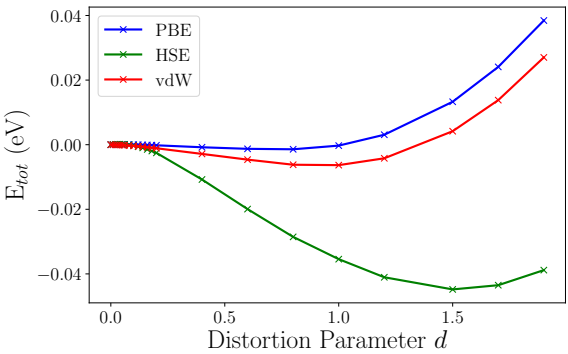

Supplementary Figure 1 Total energy calculations along the structural transition parameterized by the distortion parameter d. For all functionals their total energy change has been computed as difference to its orthorhombic value

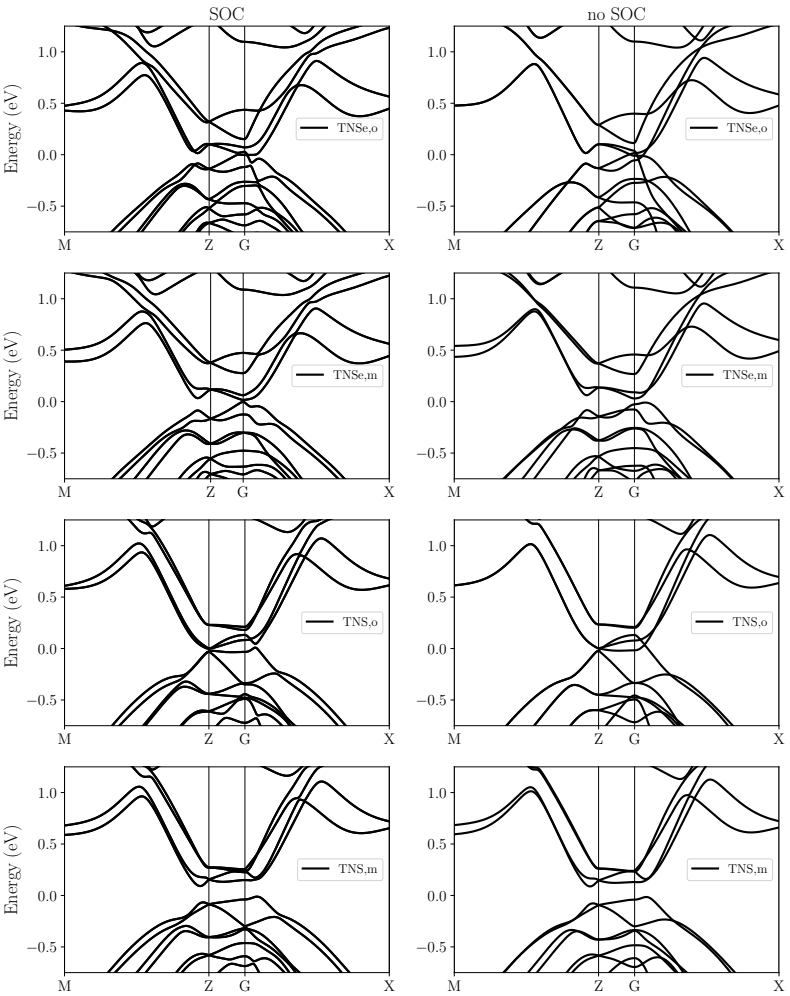

Supplementary Figure 2 Here we compare the bandstructures obtained with the PBE functional including spin orbit coupling and neglecting it for both structural phases of TNSe and TNS. The letters o and m describe the orthorhombic and monoclinic geometry in the plot labels.

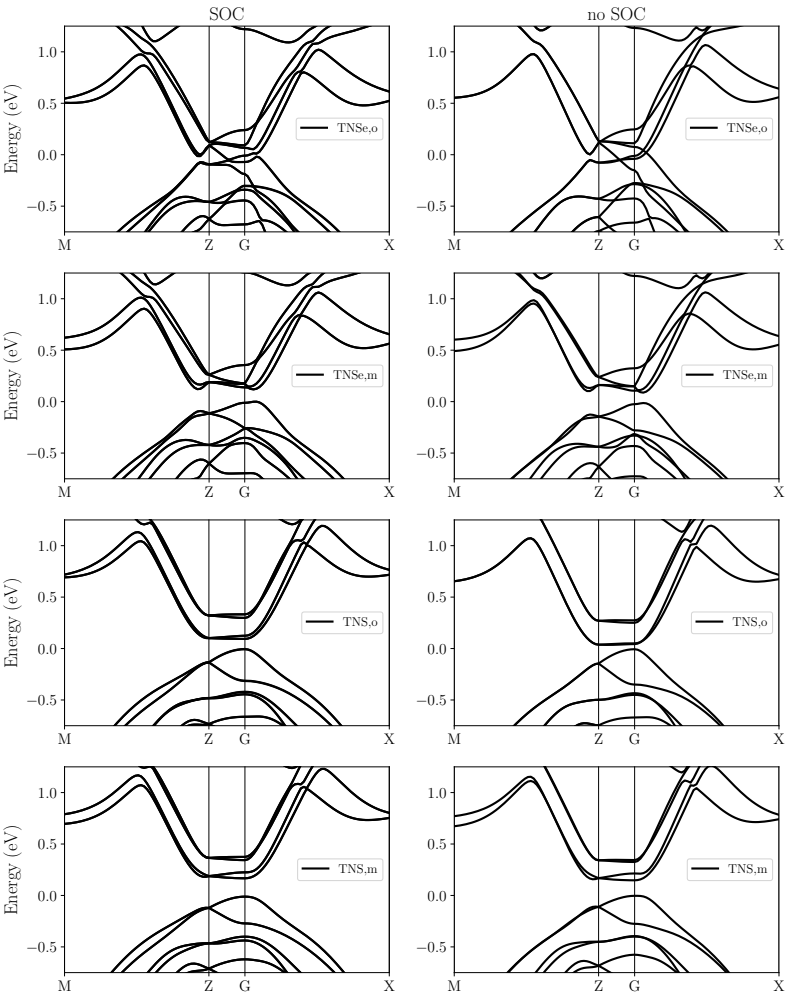

Supplementary Figure 3 Here we compare the bandstructures obtained with the mBJ functional including spin orbit coupling and neglecting it for both structural phases of TNSe and TNS. The letters o and m describe the orthorhombic and monoclinic geometry in the plot labels.

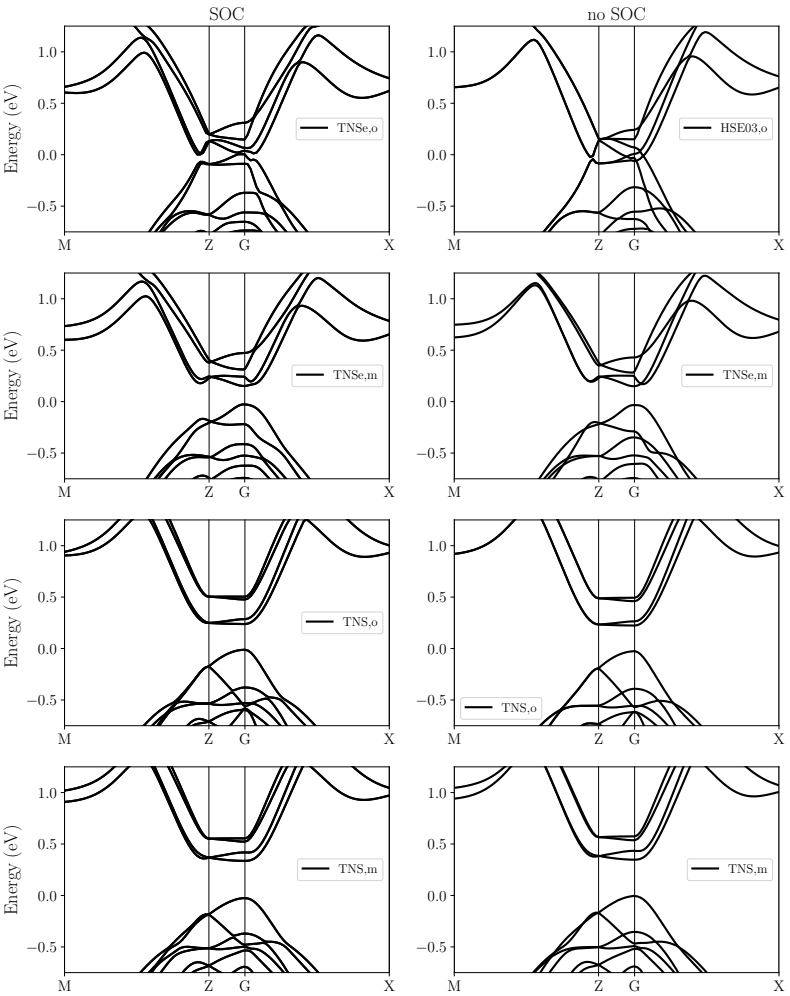

Supplementary Figure 4 Here we compare the bandstructures obtained with the HSE03 functional including spin orbit coupling and neglecting it for both structural phases of TNSe and TNS. The letters o and m describe the orthorhombic and monoclinic geometry in the plot labels.

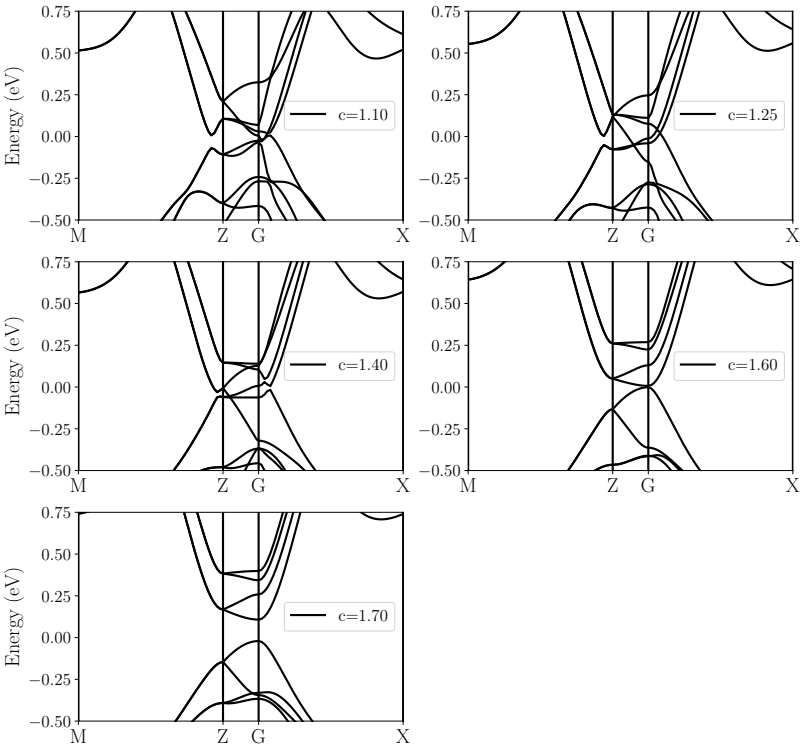

Supplementary Figure 5 Bandgap opening as we increase the amount of exchange considered in the mBJ-functional by increasing the c-parameter in the orthorhombic phase. For values higher than 1.6 a gap opens. The self consistently calculated c-Value is 1.26.

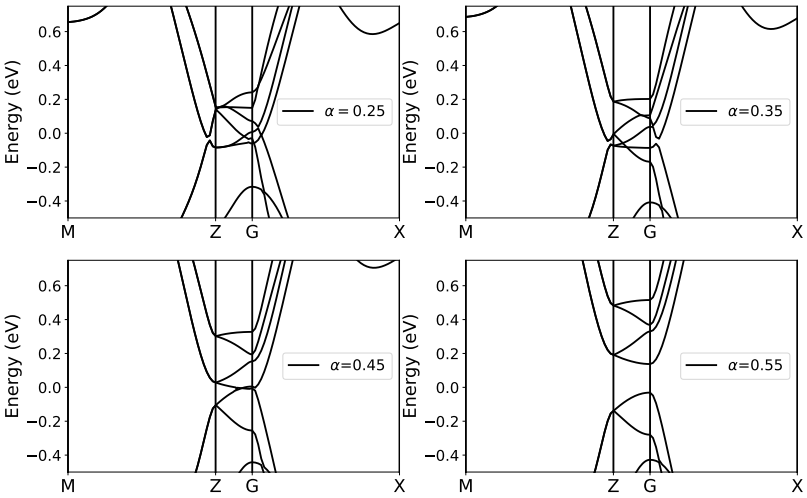

Supplementary Figure 6 Bandgap opening as we increase the amount of exchange increasing the α-parameter in the HSE hybrid functionals in the orthorhombic phase. The gap opens with increasing amount of exchange considered. The HSE03 hybrid functional corresponds to $\alpha = 0.25$. In all calculations the range separation parameter is chosen to 0.3

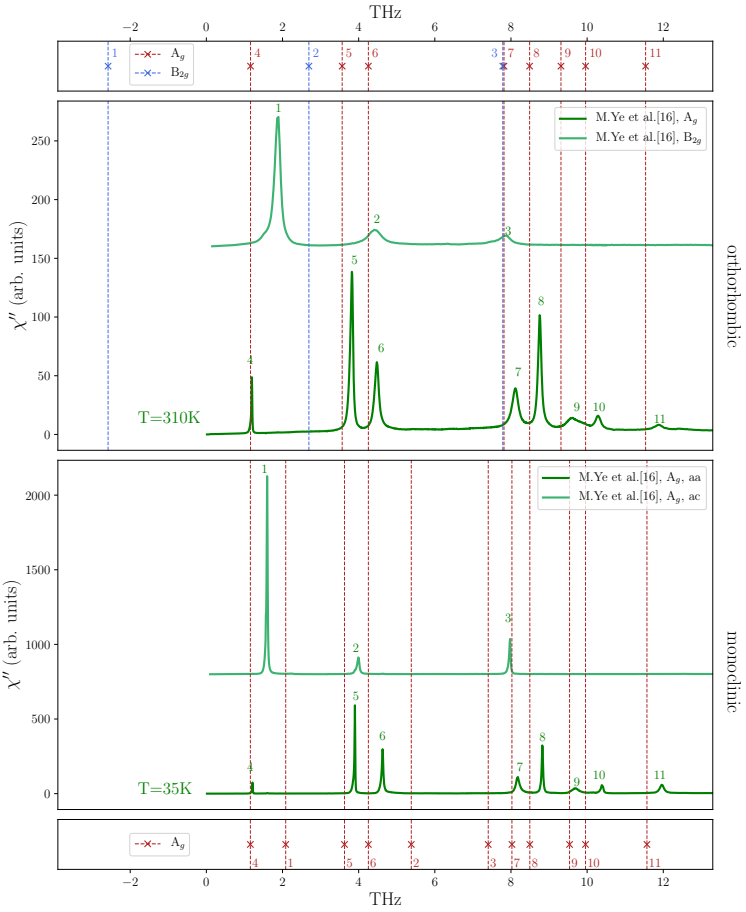

Supplementary Figure 7 Comparison of the theoretically calculated phonon eigenenergies at T=0K with the Raman spectra provided by M.Ye et al. [16] plotted on a linear scale. The top two panels show the orthorhombic phonon spectra and the bottom two panels show the monoclinic phonon spectra. The theory spectra are obtained at T=0K and are in good agreement with Raman spectra. Only the first two B_2g-modes show a relevant discrepancy in their eigenenergy.

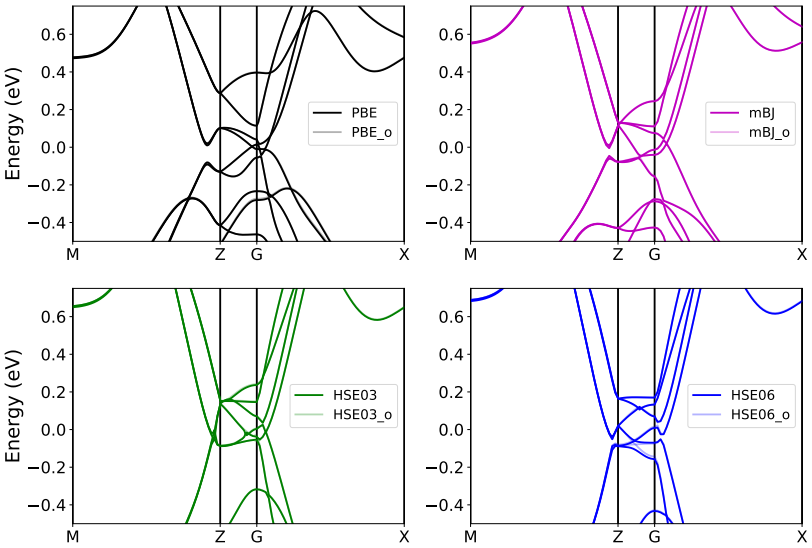

Supplementary Figure 8 Electronic Dispersion of TNSe for minimally distorted lattice geometry to break the lattice symmetries for different exchange correlation functionals (lattice distortion parameter $d = 0.05$). In shallow colors the exact orthorhombic bandstructure is displayed. We see, that for all exchange correlation functionals orthorhombic and symmetry broken dispersions are almost degenerate. We do not observe a metal to semiconductor transition or a significant gap opening for any functional.

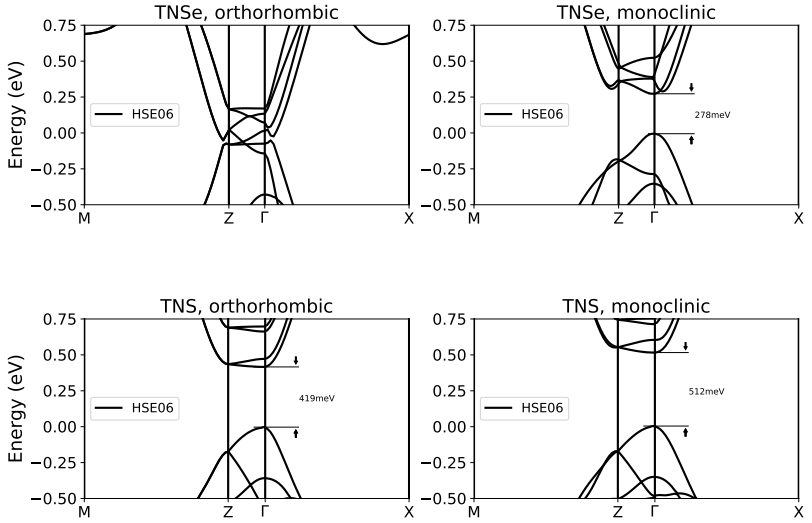

Supplementary Figure 9 Electronic Dispersion of TNSe and TNS for the orthorhombic and monoclinic geometry using the HSE06 functional.

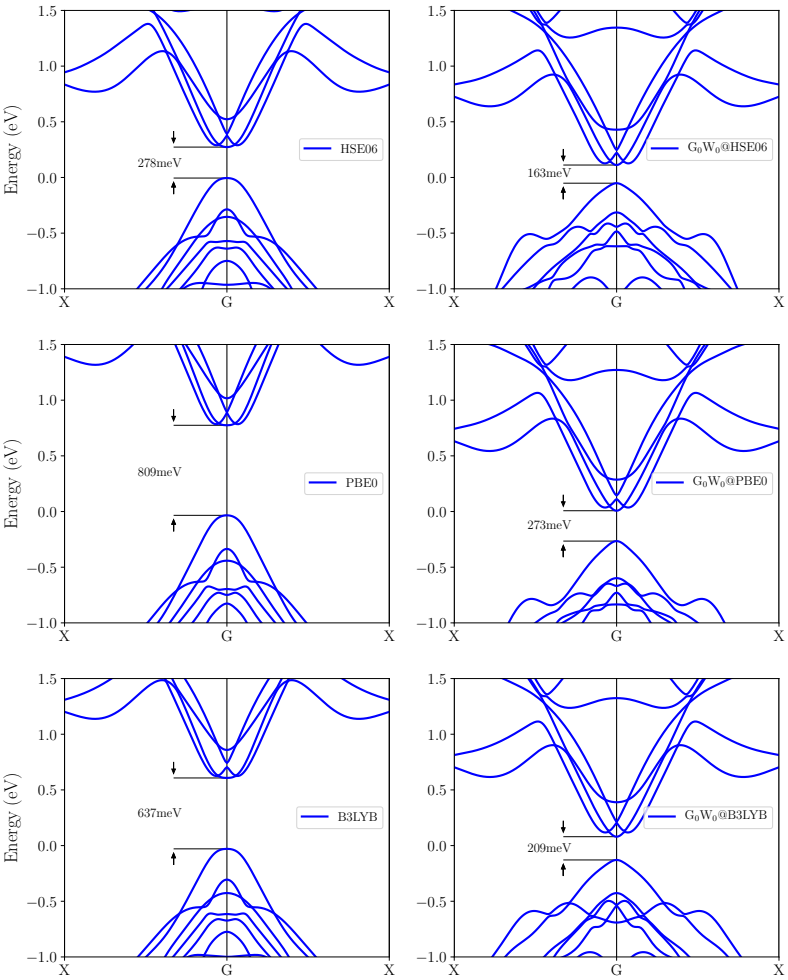

Supplementary Figure 10 Electronic Dispersion of TNSe for the monoclinic geometry using the G_0W_0 correction for different hybrid functional starting points.

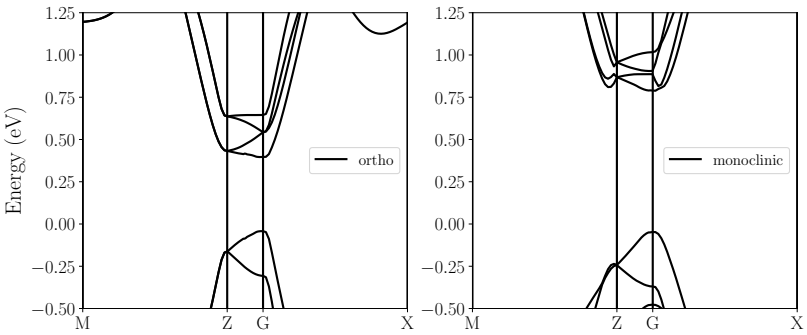

Supplementary Figure 11 Electronic Dispersion of TNSe for the orthorhombic and monoclinic geometry of TNSe using the Hartree-Fock method. The bandgaps are 438 meV for the orthorhombic and 836 meV for the monoclinic phase. Therefore, Hartree-Fock overestimates the bandgaps significantly.

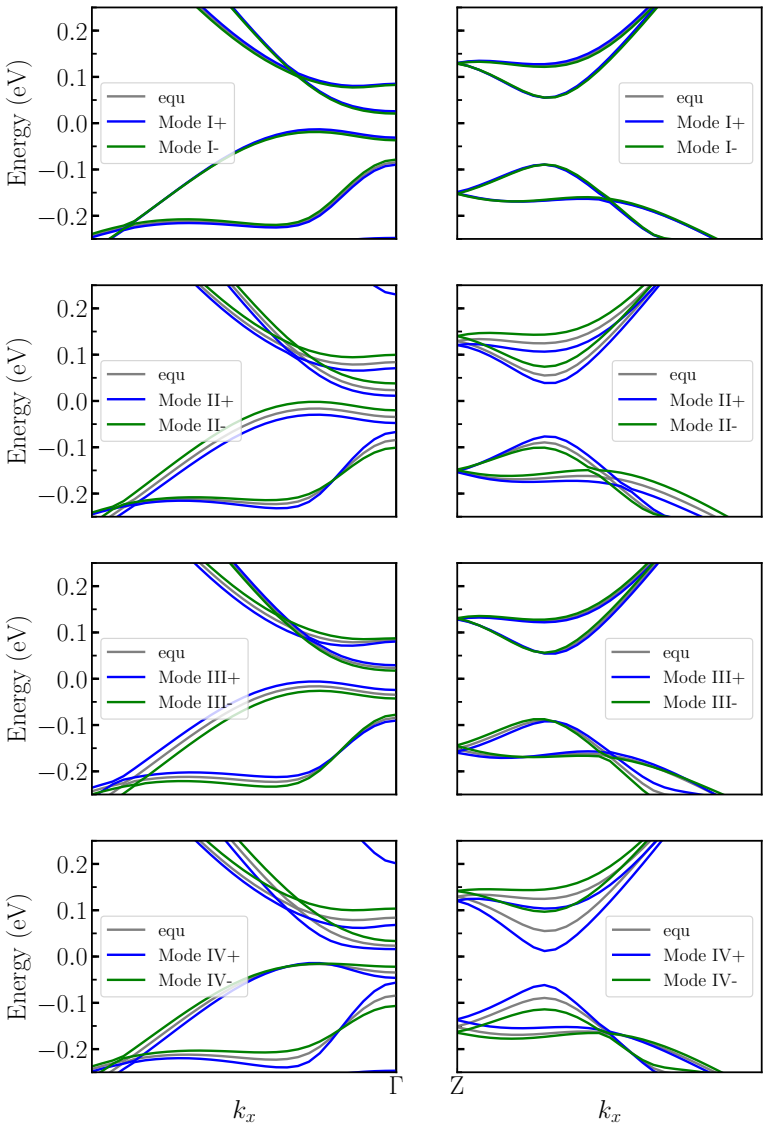

Supplementary Figure 12 Frozen phonon bandstructures after DFT calculation using the PBE functional. We displayed the result for the four Raman active phonons presented in section 5 of the main text. They show similar behavior as the results after G_0W_0 calculation. In the G_0W_0 calculation, however, the group velocity of the electrons is increased.

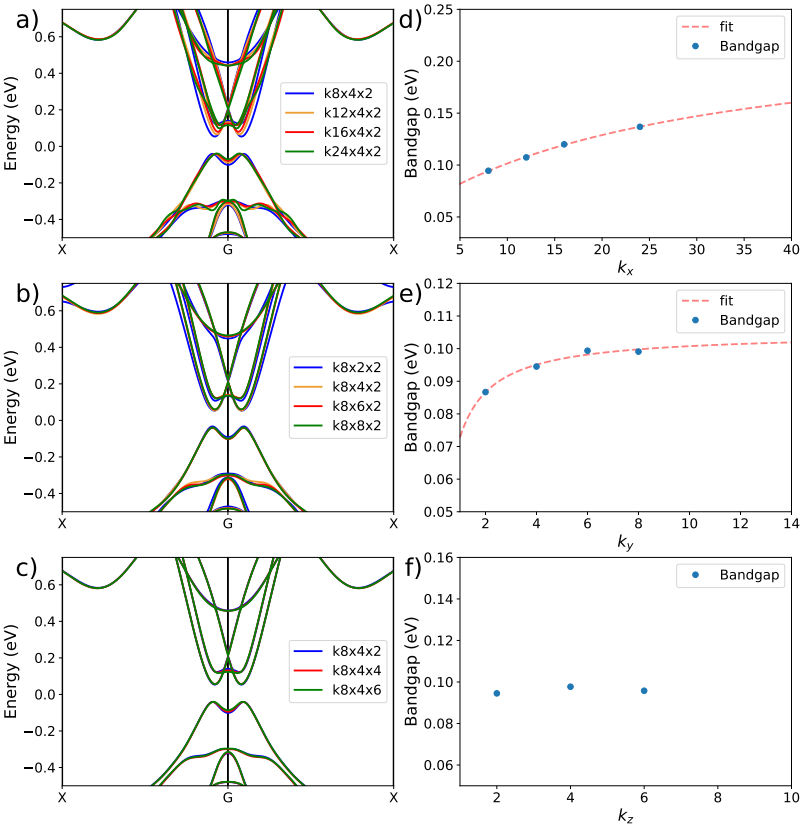

Supplementary Figure 13 Convergence of the G_0W_0 bandgap with the k-gridsize. Convergence in each direction is tested separately using 640 unoccupied states, a 80eV Cutoff for the response function and 160 frequency grid points. The panels a) - c) show the corresponding bandstructures computed with an increasing k-mesh into the different directions. the panels d)-f) show the convergence of the bandgap using increasing meshes. k_x, k_y an k_z count the number of k-points along the corresponding reciprocal lattice vector. In red dashed lines an extrapolation is displayed. In k_z direction we have too few data points for an extrapolation, but the 3 data points suggest, that convergence is already achieved for 2 points in this direction

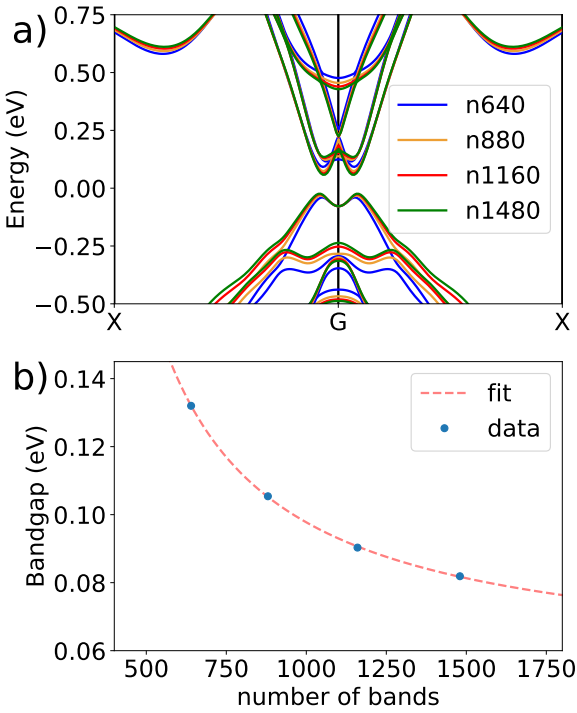

Supplementary Figure 14 G_0W_0 convergence using an increasing amount of unoccupied states while also increasing the response function cutoff simultaneously. Panel a) shows the bandstructures for an increasing number of states included in the response function calculation. Panel b) shows the convergence of the bandgap for an increasing number of orbitals included.

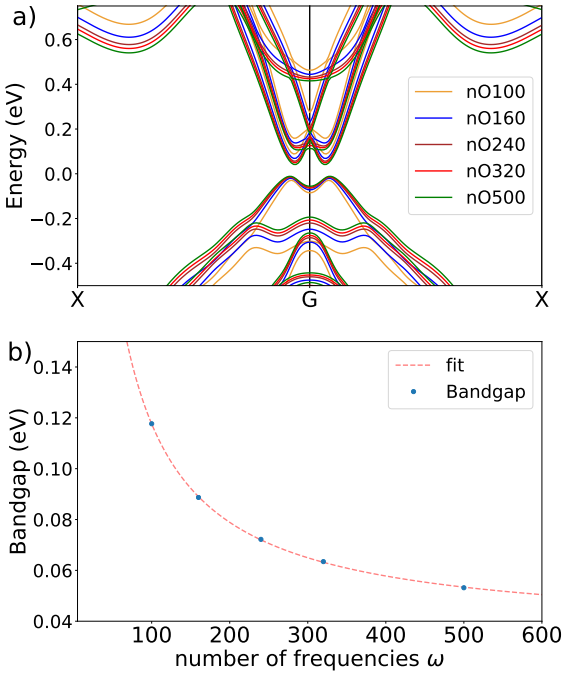

Supplementary Figure 15 G_0W_0 convergence using an increasing amount of frequencies ω. Panel a) shows the bandstructures for an increasing number of frequencies included in the screened interaction calculation. Panel b) shows the convergence of the bandgap.

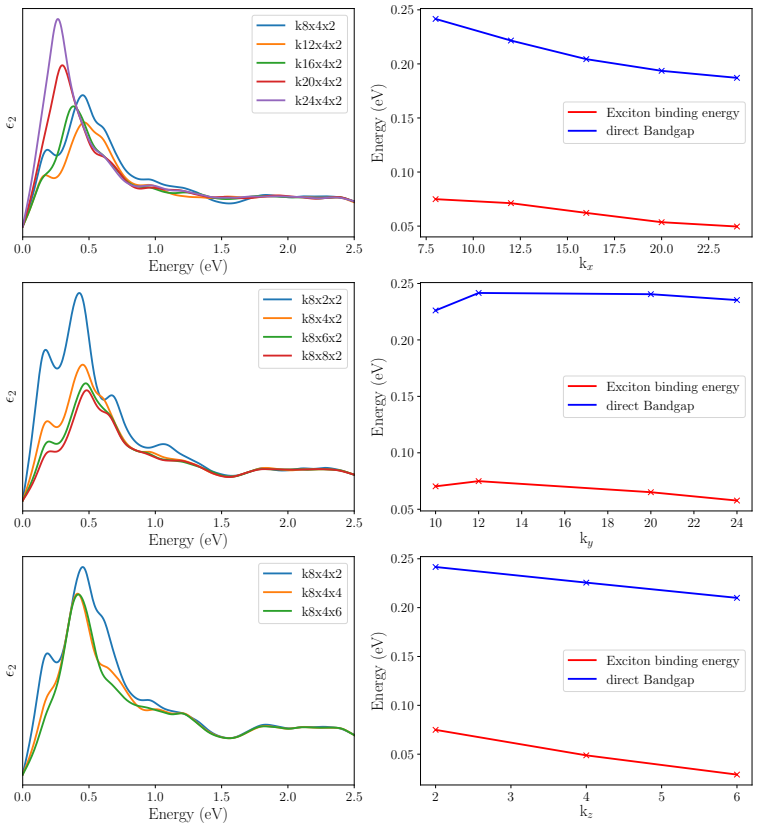

Supplementary Figure 16 Convergence of the dielectric function and BSE eigenenergies after solving the BSE using different number of k-points along the 3 axes. We see, that we need many k-Points in x-direction to obtain a converged BSE calculation. This makes sense, as we need a fine grid sampling in this direction to probe the bandgap extrema as well as its highly dispersive character in x-direction.

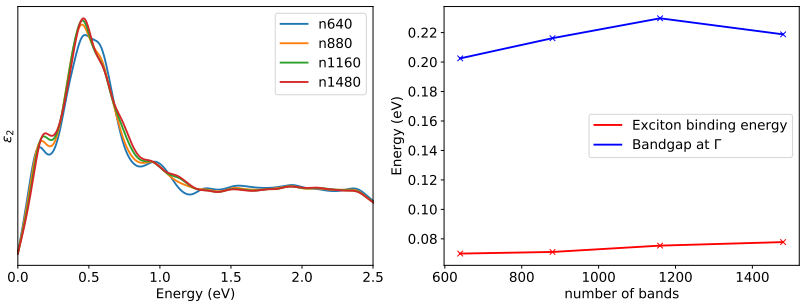

Supplementary Figure 17 Convergence of the dielectric function and BSE eigenenergies after solving the BSE using different number of unoccupied states for the calculation of the screened interaction and G_0W_0 calculation.

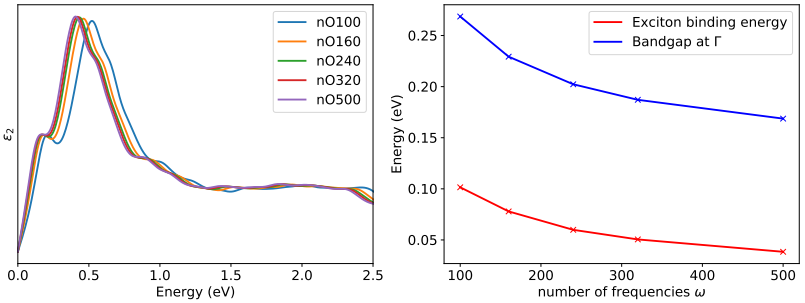

Supplementary Figure 18 Convergence of the dielectric function and BSE eigenvalues after solving the BSE using different number of frequencies for the computation of the screened interaction and the G_0W_0 calculation

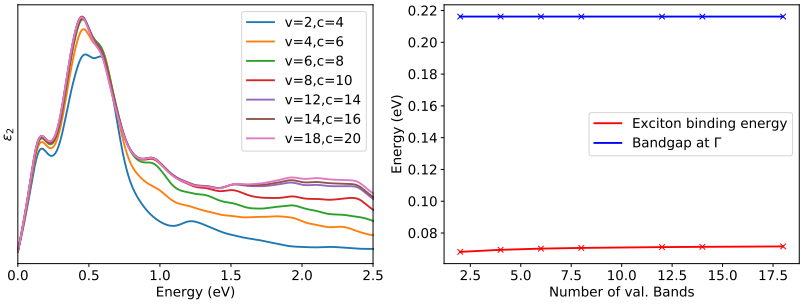

Supplementary Figure 19 Convergence of the dielectric function and first exciton energy after solving the Bethe-Salpether equation including an increasing number of valence and conduction bands. We see, that including the first 12 valence and 14 conduction bands results in a well converged dielectric function and excitonic energies.

Supplementary References

[1] Sugimoto, K., Nishimoto, S., Kaneko, T. & Ohta, Y. Strong coupling nature of the excitonic insulator state in Ta_2NiSe_5. *Phys. Rev. Lett.* **120**, 247602 (2018) .

[2] Becke, A. D. & Johnson, E. R. A simple effective potential for exchange. *J. Chem. Phys.* **124** (22), 221101 (2006). https://doi.org/10.1063/1.2213970 .

[3] Becke, A. D. & Roussel, M. R. Exchange holes in inhomogeneous systems: A coordinate-space model. *Phys. Rev. A* **39**, 3761–3767 (1989) .

[4] Tran, F. & Blaha, P. Accurate band gaps of semiconductors and insulators with a semilocal exchange-correlation potential. *Phys. Rev. Lett.* **102**, 226401 (2009) .

[5] Heyd, J., Scuseria, G. E. & Ernzerhof, M. Hybrid functionals based on a screened coulomb potential. *J. Chem. Phys.* **118** (18), 8207–8215 (2003) .

[6] Lee, J. *et al.* Strong interband interaction in the excitonic insulator phase of Ta_2NiSe_5. *Phys. Rev. B* **99**, 075408 (2019) .

[7] Lu, Y. F. *et al.* Zero-gap semiconductor to excitonic insulator transition in Ta_2NiSe_5. *Nat. Commun.* **8** (1) (2017) .

[8] Sunshine, S. A. & Ibers, J. A. Structure and physical properties of the new layered ternary chalcogenides tantalum nickel sulfide (Ta_2NiS_5) and tantalum nickel selenide (Ta_2NiSe_5). *Inorg. Chem.* **24** (22), 3611–3614 (1985) .

[9] Nakano, A. *et al.* Antiferroelectric distortion with anomalous phonon softening in the excitonic insulator Ta_2NiSe_5. *Phys. Rev. B* **98**, 045139 (2018) .

[10] Klimeš, J. c. v., Kaltak, M. & Kresse, G. Predictive gw calculations using plane waves and pseudopotentials. *Phys. Rev. B* **90**, 075125 (2014) .

[11] Mostofi, A. A. *et al.* An updated version of wannier90: A tool for obtaining maximally-localised wannier functions. *Comput. Phys. Commun.* **185** (8), 2309 – 2310 (2014) .

[12] Salpeter, E. E. & Bethe, H. A. A relativistic equation for bound-state problems. *Phys. Rev.* **84**, 1232–1242 (1951) .

[13] Sander, T., Maggio, E. & Kresse, G. Beyond the tamm-dancoff approximation for extended systems using exact diagonalization. *Phys. Rev. B* **92**, 045209 (2015) .

[14] Dancoff, S. M. Non-adiabatic meson theory of nuclear forces. *Phys. Rev.* **78**, 382–385 (1950) .

[15] Nakano, A. *et al.* Pressure-induced coherent sliding-layer transition in the excitonic insulator Ta_2NiSe_5. *IUCrJ* **5** (2), 158–165 (2018) .

[16] Ye, M. *et al.* Lattice dynamics of the excitonic insulator $Ta_2Ni(Se_{1-x}S_x)_5$. *Phys. Rev. B* **104**, 045102 (2021) .